

# Global Control for Local $SO(3)$ -Equivariant Scale-Invariant Vessel Segmentation

Patryk Rygiel<sup>\*1</sup>[0009-0003-8539-5581], Dieuwertje Alblas<sup>\*1</sup>[0000-0002-7754-7405],  
 Christoph Brune<sup>1</sup>[0000-0003-0145-5069],  
 Kak Khee Yeung<sup>2,3</sup>[0000-0002-8455-286X], and  
 Jelmer M. Wolterink<sup>1</sup>[0000-0001-5505-475X]

<sup>1</sup> Department of Applied Mathematics, Technical Medical Centre, University of Twente, Enschede, The Netherlands

{p.t.rygiel,d.alblas,c.brune,j.m.wolterink}@utwente.nl

<sup>2</sup> Department of Surgery, Amsterdam UMC location Vrije Universiteit Amsterdam, Amsterdam, The Netherlands

<sup>3</sup> Amsterdam Cardiovascular Sciences, Microcirculation, Amsterdam, The Netherlands

**Abstract.** Personalized 3D vascular models can aid in a range of diagnostic, prognostic, and treatment-planning tasks relevant to cardiovascular disease management. Deep learning provides a means to automatically obtain such models. Ideally, a user should have control over the exact region of interest (ROI) to be included in a vascular model, and the model should be watertight and highly accurate. To this end, we propose a combination of a global controller leveraging voxel mask segmentations to provide boundary conditions for vessels of interest to a local, iterative vessel segmentation model. We introduce the preservation of scale- and rotational symmetries in the local segmentation model, leading to generalisation to vessels of unseen sizes and orientations. Combined with the global controller, this enables flexible 3D vascular model building, without additional retraining. We demonstrate the potential of our method on a dataset containing abdominal aortic aneurysms (AAAs). Our method performs on par with a state-of-the-art segmentation model in the segmentation of AAAs, iliac arteries and renal arteries, while providing a watertight, smooth surface segmentation. Moreover, we demonstrate that by adapting the global controller, we can easily extend vessel sections in the 3D model.

**Keywords:** vessels · segmentation · cardiovascular · geometric deep learning · scale-invariance · rotation-equivariance · data efficiency

## 1 Introduction

Detailed and topologically correct 3D vascular models can aid in many diagnostic, prognostic, and treatment-planning tasks in patients with cardiovascular

---

\* Equal contribution.

diseases. Examples include diameter measurements in aneurysms [5], tortuosity measurements [7], fitting stent grafts [13], or hemodynamic analysis with computational fluid dynamics (CFD) [22]. Automatically obtaining 3D models for these purposes has long been a topic of interest [14] that has been primarily targeted with deep learning (DL) recently [6,15].

Most current DL methods for 3D vessel segmentation perform voxel segmentation. These models interpret the *global* context of the image and yield a 3D voxel mask of the vessels, e.g., [10,19]. However, the topological correctness of such voxel masks can only be imposed as a soft constraint [21]. Moreover, the resolution of voxel masks is limited to that of the scanner, which for downstream tasks such as CFD is often insufficient. Alternatively, vessels can be parametrized as generalized cylinders consisting of a manually or automatically [24,8,4] identified centerline and a set of *locally* orthogonal contours [20]. This parametrization has been successfully integrated into machine learning approaches that achieve sub-voxel accuracy [16,25,2]. Such local methods can more naturally incorporate rotational and scale symmetries present in vessels [4,2] to learn efficiently from few annotations. In contrast to voxel masks, a generalized cylinder always yields a locally topologically correct representation of the vessel. However, a drawback of local tracking and segmentation is the lack of global context, making it difficult to detect the intended region of interest (ROI) for segmentation. When the user is interested in only a particular segment of the vasculature, stopping criteria based on local heuristics [24,12,8] are unable to constrain a local model without global information.

In this work, we unify global and local segmentation approaches by introducing a global controller for a local segmentation model. Open source multi-organ segmentation models like TotalSegmentator [23] are a useful commodity for the community that we here leverage to provide a set of *global* boundary conditions to guide *local* tracking and segmentation. This gives us the best of both worlds: we can select only those parts of the vasculature that are relevant to a particular task, and we can exploit local symmetries in vessel segmentation to obtain generalizable models with sub-voxel accuracy. Specifically, we introduce scale-invariant and rotation-equivariant local segmentation, which generalizes between vessels with very different calibres. We reconstruct smooth and watertight surfaces for each artery by fitting a neural field to the contours resulting from the local segmentation [3] and blend these surfaces into watertight meshes of the vasculature. We demonstrate the effectiveness of our method on a dataset of patients with abdominal aortic aneurysms (AAAs), where we obtain topologically correct and smooth models of the renal arteries, iliac arteries, and abdominal aorta based on limited training data. Moreover, we show how the user can effectively control the segmentation ROI. Our results show that global and local segmentation are not mutually exclusive, but can be combined in a fruitful synergy to add value for cardiovascular disease management.

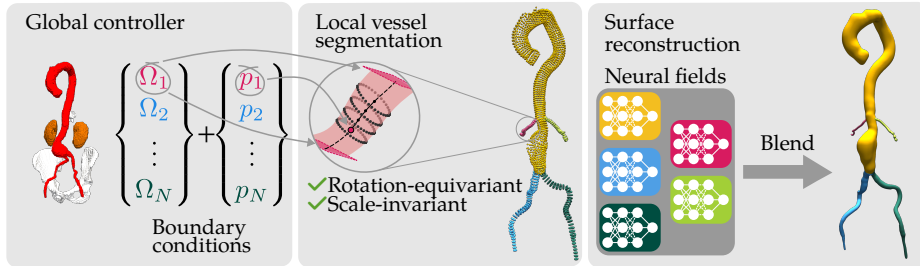


**Fig. 1.** Proposed framework. A global segmentation or localization method is used to provide boundary conditions  $[\Omega_i, p_i]$ , such as points or regions-of-interest (ROIs) for the global control of local vessel segmentation. A local joint tracking and segmentation model accurately segments vessels in a rotation-equivariant, scale-invariant manner. Obtained contour sets are reconstructed into a watertight surface using neural fields and blended into a single vascular model [3].

## 2 Materials & Methods

Figure 1 visualizes our framework, consisting of three elements: (1) extraction of boundary conditions for a global controller, (2) iterative local vessel segmentation subject to these boundary conditions and (3) reconstruction of a smooth watertight surface.

### 2.1 Global controller

The iterative local vessel tracker used to extract topologically correct vessel contours lacks a global overview and hence does not know where to start or terminate. In previous works, starting points were sampled from segmentation mask and stopping criteria were based on heuristics intrinsic to the tracker [4,24], but this often resulted in early stopping or roaming of the tracker. Instead, we use coarse segmentations of TotalSegmentator [23], an off-the-shelf multi-organ segmentation algorithm, as a global controller for the precise and topologically accurate iterative vessel segmentation module. For each vessel of interest  $v_i$  in our 3D vascular model, we use this coarse segmentation to determine the boundary conditions, i.e. a seed point  $p_i$  and the set of stopping criteria  $\Omega_i$ .

### 2.2 Local vessel tracking and segmentation

From a local perspective, vessel appearance is subject to change due to varying orientations and diameters of the vessel. For example, the diameters of renal arteries are around 5 mm, iliac arteries range around 10 mm, while AAAs with diameters 80 mm are not uncommon [1]. This poses a challenge to local artery segmentation methods that use image patches of fixed resolution and size, e.g. [25,16]. A local segmentation method that is unaffected by vessel diameter and orientation is thus desirable.

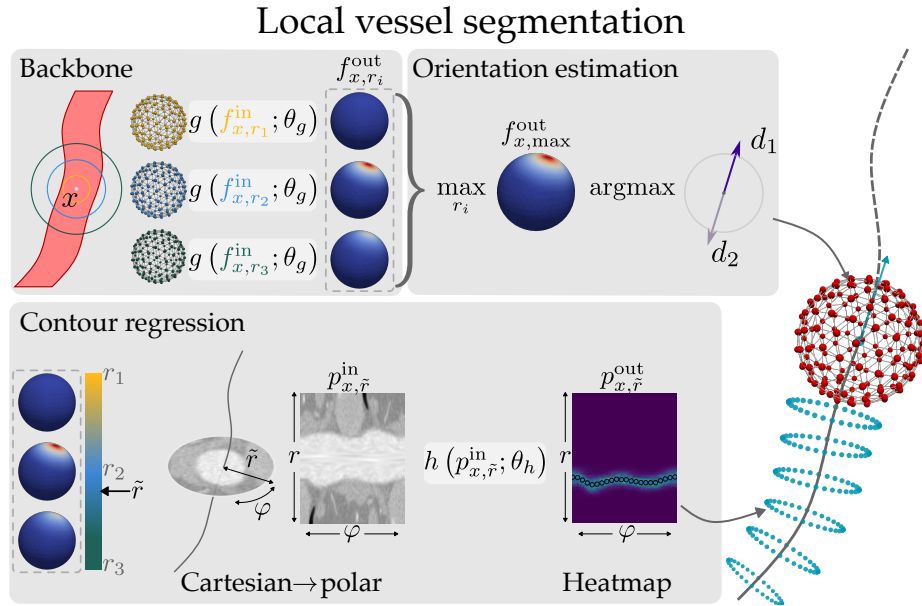


**Fig. 2.** Overview of our iterative segmentation method, consisting of two steps. (1) At a point  $x$ , local vessel orientations are determined based on multi-scale spherical image features. (2) Based on the multi-scale responses, the optimal scale  $\tilde{r}$  is selected, from which a scale-adaptive polar image normal to the local vessel orientation is constructed. CNN  $h(\cdot; \theta_h)$  predicts lumen radii for each angle in  $p_{\tilde{r}}^{\text{in}}$ , forming a closed contour in Cartesian space.

We propose a scale-invariant, rotation-equivariant local segmentation module that performs iterative joint tracking and segmentation of the vessel, using its cylindrical shape as an anatomical prior. To track vessel  $v_i$ , the module is initialized at seed point  $p_i$ , provided by the global controller. First, the module estimates up- and downstream vessel directions  $\mathbf{d}_1$  and  $\mathbf{d}_2$  at  $p_i$ . Subsequently, the vessel takes a step of size  $\Delta$  in direction  $\mathbf{d}_1$ . Every  $\eta$  steps, the module delineates the lumen boundary orthogonal to the local vessel orientation. These two steps are shown in Figure 2. Once one of the vessel-specific boundary conditions in  $\Omega_i$  is violated, the tracker terminates. If direction  $\mathbf{d}_2$  is not yet explored, the tracker is re-initialized at  $p_i$  and traverses the vessel in direction  $\mathbf{d}_2$  until termination. Both resulting centerline paths are combined into one centerline.

Both steps of the iterative segmentation rely on a scale-invariant, rotation-equivariant backbone [4], which extracts features from image data centered around a point  $x \in \mathbb{R}^3$  (top-left Fig. 2). This backbone consists of a graph convolutional network (GCN) [11]  $g(\cdot; \theta_g)$  operating on the surface of the unit sphere on which local image information within a predefined radius  $r$  of  $x$  has been projected ( $f_{x,r}^{\text{in}}$ ). The backbone outputs a scalar field  $f_{x,r}^{\text{out}}$  on the unit sphere. To adapt to vessels of different calibres, the backbone processes local image in-

formation at different scales in parallel. We construct a set of multi-scale inputs  $\{f_{x,r_j}^{\text{in}}\}_{j=1,\dots,m}$  from a pre-defined set of  $m$  scales  $R = \{r_j\}_{j=1,\dots,m}$  that we feed through  $g(\cdot; \theta_g)$ . This results in a set of multi-scale outputs  $\{f_{x,r_j}^{\text{out}}\}_{j=1,\dots,m}$ , which are used by the orientation estimation and contour regression modules.

The vessel orientation estimation first aggregates  $\{f_{x,r_j}^{\text{out}}\}_{j=1,\dots,m}$  into a scale-invariant output  $f_{x,\text{max}}^{\text{out}}$  by using a permutation-invariant maximum operation across the scales (top-right Fig. 2) [4]. The local orientations  $\mathbf{d}_1$  and  $\mathbf{d}_2$  of the vessel at  $x$  are represented by the locations of  $f_{x,\text{max}}^{\text{out}}$ , at least  $90^\circ$  apart.

The contour regression module yields a closed contour delineating the lumen boundary on a 2D plane through  $x$  orthogonal to the centerline, while adapting to the vessel calibre (bottom Fig. 2). Closed contours are enforced by estimating the lumen radius for each angle on a polar transformed image  $p_{x,\tilde{r}}^{\text{in}} \in \mathbb{R}^{N_r \times N_\varphi}$ , centered at  $x$  with radius  $\tilde{r}$  [2]. Instead of using polar images with fixed  $\tilde{r}$  as in [2], we adapt the radius  $\tilde{r}$  to the local vessel size, by computing it as the weighted average of the maximum activations on each scale-wise response in  $\{f_{x,r_j}^{\text{out}}\}_{j=1,\dots,m}$ . Next, a CNN  $h(\cdot; \theta_h)$  predicts a heatmap  $p_{x,\tilde{r}}^{\text{out}} \in \mathbb{R}^{N_r \times N_\varphi}$ , where locations of maxima along each column correspond to the lumen radius. We extract the lumen contour from  $p_{x,\tilde{r}}^{\text{out}}$  differentiably, hence  $h(\cdot; \theta_h)$  can be optimized using a set of ground-truth contours [18,9]. Network  $h(\cdot; \theta_h)$  is translation equivariant and operates on a polar transformed image, implying rotational equivariance in Cartesian space: a rotation of the 2D input plane leads to the same rotation of the output contour.

### 2.3 Surface reconstruction

Iterative tracking results in a set of contours that locally describes the lumen surface of vessel  $v_i$ , but is not watertight. To reconstruct the surface subject to these contours, we use a neural field (right Fig. 1). This neural field consists of a multi-layer perceptron that is conditioned on spatial coordinates  $x \in \mathbb{R}^3$  and is optimized to represent the signed distance function of the lumen surface [17]. As these neural fields are conditioned on continuous coordinates, they have an infinite resolution. Moreover, a smooth transition between connecting vessels is made by taking a smoothed minimum of their signed distance functions [3]. From the neural field, we can obtain a mesh model of any resolution using the marching cubes algorithm.

### 2.4 Data

We use an in-house dataset consisting of 80 pre-operative contrast-enhanced CT (CTA) scans of AAA patients obtained from Amsterdam UMC, containing at least the thoracic region until the iliac bifurcation. In-plane resolutions and slice thicknesses range between 0.6-1.0 mm and 0.5-2.0 mm, respectively. For each patient, we obtained manual annotations consisting of centerlines and locally orthogonal contours of the lumen of the abdominal aorta until the top of the T12 vertebra, the common iliac arteries, and the renal arteries.

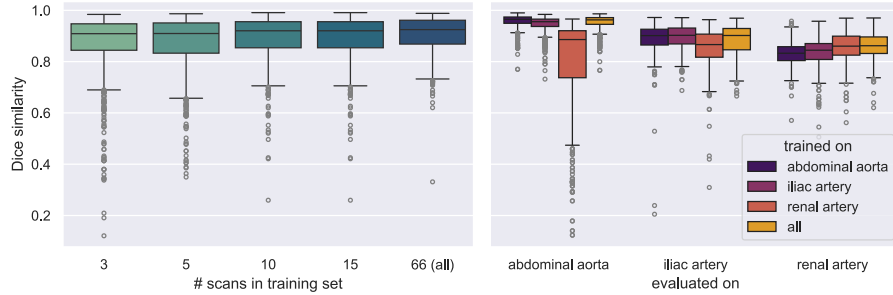


**Fig. 3.** DSC scores of the contour regression modules on 2D contours in the test set for the data ablation experiments. *Left:* DSC for all contours for data ablation at patient level. *Right:* DSC per vessel for data ablation at the vessel level.

### 3 Experiments & Results

We split the 80 AAA patients into 14 test cases and used the remaining 66 cases to train the two networks in the local vessel segmentation module. We denote the orientation estimation module as  $\mathcal{T} = \{g(\cdot; \theta_g)\}$  and the contour regression module as  $\mathcal{S} = \{g(\cdot; \theta_g), h(\cdot; \theta_h)\}$ . Note that the orientation estimation and contour regression are trained separately. Both  $\mathcal{T}$  and  $\mathcal{S}$  were trained with an Adam optimizer, with learning rates of 0.005, 0.001 and batch sizes of 20 and 10 respectively. For both training and inference, we used scales  $R = \{5, 10, 15, \dots, 80\}$  for the backbone. For tracking we use step sizes  $\Delta_{aorta} = 1$  mm,  $\Delta_{iliac} = 0.5$  mm,  $\Delta_{renal} = 0.3$  mm and constant  $\eta = 5$ .

The global controller provided seed points and boundary conditions for tracking the abdominal aorta, iliac arteries and renal arteries. Unless stated otherwise, we used the following heuristics for  $p_i$  and  $\Omega_i$ .  $p_{aorta}$  and  $p_{iliac}$  are the centers of mass from the aorta and iliac masks provided by TotalSegmentator, respectively.  $p_{renal}$  is a bit more challenging to obtain, as TotalSegmentator does not include renal arteries. Instead, we estimate the renal artery by computing the shortest path between the kidneys and the aorta based on image intensities, and let  $p_{renal}$  be the center of this path.  $\Omega_{aorta}$  consists of the region above the T12 vertebra and the iliac artery segmentations,  $\Omega_{iliac}$  contains the aorta and the region below the L5 vertebra, and  $\Omega_{renal}$  contains the kidneys and the aorta.

#### 3.1 Segmentation quality

We evaluate the quality of the automatically extracted 3D vascular models on the test set. For each of the 14 test cases, we automatically extract the lumen of the abdominal aorta, renal arteries, and iliac arteries. We compare the quality of these segmentations to an nnU-Net benchmark. We obtained Dice similarity coefficients of  $0.84 \pm 0.05$  and  $0.83 \pm 0.14$  for our method and nnU-Net, respectively, demonstrating that we can fully automatically obtain watertight meshes

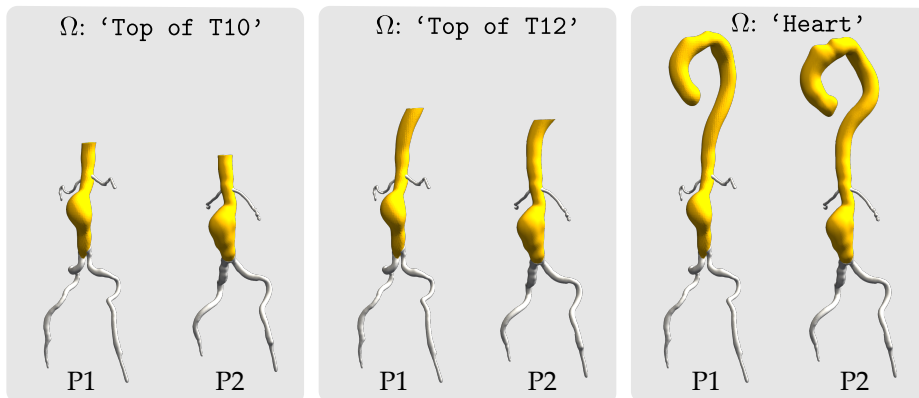


Fig. 4. Automatically acquired 3D vascular models using different  $\Omega_{\text{aorta}}$ .

with sub-voxel accuracy without compromising on overlap metrics. However, we did observe that sometimes  $p_{\text{renal}}$  is not accurately found, resulting in missing branches in our model.

### 3.2 Data efficiency

We train our iterative vessel segmentation method using 2D images with annotated contours. Therefore, a single 3D scan can contain hundreds of training samples. This - in combination with the symmetries that we embed - makes our method very data efficient. We retrained the contour regression model on subsets of 3, 5, 10, and 15 patients randomly selected from the training set to assess this data efficiency. We evaluate the performance of each model using the DSC on the 2D contours in the test set. Figure 3 (left) shows the results of this experiment. We observe that the performance of the contour regression module is quite stable, even when it was trained on only three patients.

As the contour regression module is scale-invariant, it should generalise to vessels of unseen calibre. To test this property, we perform data ablation at the artery level. We retrain three contour regression modules separately on the lumen contours of the abdominal aorta, iliac arteries, and renal arteries, whose diameters range between 20-55 mm, 10-15 mm, and 5-7 mm, respectively. We assess the performance of the four models using the DSC on the 2D contours of the test set. Figure 3 (right) shows that overall, our model can generalise to arteries of unseen size. For example, we see that the model trained on abdominal aorta contours performs on par with the model trained on iliac arteries when segmenting iliac arteries and vice versa. Moreover, the model trained on all arteries shows comparable performance to the vessel-specific model, indicating that heterogeneity of vessel size in the training data does not deteriorate segmentation performance. However, we observe a performance drop for segmentation of the abdominal aorta for the model trained on renal arteries.

### 3.3 Modifying boundary conditions

The global controller we present provides flexible incorporation of custom sections of vessels to include in the 3D vascular model. To demonstrate this, we extract 3D models while adapting  $\Omega_{aorta}$ . We include three different regions in  $\Omega_{aorta}$  to terminate iterative segmentation in the superior direction: above the top of the T10 vertebra, above the top of the T12 vertebra, and the heart. Figure 4 shows visualizations of the resulting 3D vascular models. Although the iterative tracker was trained only on contours of the abdominal aorta between the T12 vertebra and iliac bifurcation, it still tracks and segments the aortic arch due to its symmetry-preserving properties.

## 4 Conclusion & Discussion

We have presented a general framework for automatically extracting smooth, topologically correct vascular models, combining strengths of global and local vessel segmentation methods. A global controller provides boundary conditions for a local iterative vessel segmentation model, that exploits local scale- and rotational symmetries to generalise to vessels of unseen sizes and orientations. Our post-processing step provides a neural field of the vascular model that can be reconstructed to a mesh of any desired resolution. We demonstrated the effectiveness of symmetry preservations by automatic extraction of vascular models of abdominal aortic aneurysms, iliac arteries and renal arteries.

By leveraging local scale- and rotational symmetries, our iterative joint tracking and segmentation module generalizes to vessels of sizes (Fig. 3, left) and sections (Fig. 4) unseen during training. Despite this strong generalisation, some symmetries cannot be preserved. For example, the contour regression model trained on renal arteries struggles to segment the abdominal aorta lumen if surrounded by a thrombus, as this was not seen during training. Moreover, generalisation to other image modalities, e.g. MRI or ultrasound requires retraining. However, as the local vessel segmentation step can be trained on contour annotations of a few patients, data collection and annotation costs are low.

The global controller we present in this work gives the user control over which vessel sections to incorporate in the final vascular model. In combination with the generalising properties of the iterative tracker, this allows to automatically build 3D vascular models in other anatomical regions by providing a different set of heuristics. We used segmentation masks from TotalSegmentator [23] as input for our global controller, an off-the-shelf tool. In combination with the generalising local segmentation method, it has the potential to automatically segment any vascular region without the need for additional specific annotations. Nevertheless, another model could be added to provide more specialized boundary conditions for tracking, e.g. for  $p_{renal}$  in our experiments. Moreover, as all vessel segments are tracked separately using their own set of predefined boundary conditions, the vascular model is fully labelled. As the boundary conditions for each artery are standardized, the regions of interest of the resulting 3D vascular models are consistent across subjects. This enables large-scale studies of the role

of hemodynamic and morphological features in the prognosis of cardiovascular diseases.

In conclusion, we have shown that global constraints can be imposed on local tracking and segmentation models to provide high-quality watertight segmentations of the vasculature.

**Acknowledgments:** This project has received funding from the European Union’s Horizon Europe research and innovation programme under grant agreement No 101080947 (VASCUL-AID). Jelmer M. Wolterink was supported by the NWO domain Applied and Engineering Sciences Veni grant (18192).

## References

1. Aggarwal, S., Qamar, A., Sharma, V., Sharma, A.: Abdominal aortic aneurysm: A comprehensive review. *Experimental & Clinical Cardiology* **16**(1), 11 (2011)
2. Alblas, D., Brune, C., Wolterink, J.M.: Deep learning-based carotid artery vessel wall segmentation in black-blood mri using anatomical priors (2021)
3. Alblas, D., Brune, C., Yeung, K.K., Wolterink, J.M.: Going off-grid: continuous implicit neural representations for 3d vascular modeling. In: *International Workshop on Statistical Atlases and Computational Models of the Heart*. pp. 79–90. Springer (2022)
4. Alblas, D., Suk, J., Brune, C., Yeung, K.K., Wolterink, J.M.: Sire: scale-invariant, rotation-equivariant estimation of artery orientations using graph neural networks (2023)
5. Brewster, D.C., Cronenwett, J.L., Hallett, Jr, J.W., Johnston, K.W., Krupski, W.C., Matsumura, J.S., Joint Council of the American Association for Vascular Surgery and Society for Vascular Surgery: Guidelines for the treatment of abdominal aortic aneurysms. report of a subcommittee of the joint council of the american association for vascular surgery and society for vascular surgery. *J Vasc Surg* **37**(5), 1106–1117 (May 2003)
6. Chen, C., Qin, C., Qiu, H., Tarroni, G., Duan, J., Bai, W., Rueckert, D.: Deep learning for cardiac image segmentation: a review. *Frontiers in Cardiovascular Medicine* **7**, 25 (2020)
7. Ciuricǎ, S., Lopez-Sublet, M., Loeys, B.L., Radhouani, I., Natarajan, N., Vikkula, M., Maas, A.H., Adlam, D., Persu, A.: Arterial tortuosity: novel implications for an old phenotype. *Hypertension* **73**(5), 951–960 (2019)
8. Friman, O., Hindennach, M., Kühnel, C., Peitgen, H.O.: Multiple hypothesis template tracking of small 3d vessel structures. *Medical image analysis* **14**(2), 160–171 (2010)
9. Gajowczyk, M., Rygiel, P., Grodek, P., Korbecki, A., Sobanski, M., Podgorski, P., Konopczynski, T.: Coronary ostia localization using residual u-net with heatmap matching and 3d dsnt. In: Lian, C., Cao, X., Rekić, I., Xu, X., Cui, Z. (eds.) *Machine Learning in Medical Imaging*. pp. 318–327. Springer Nature Switzerland, Cham (2022)
10. Gharlegghi, R., Adikari, D., Ellenberger, K., Ooi, S.Y., Ellis, C., Chen, C.M., Gao, R., He, Y., Hussain, R., Lee, C.Y., et al.: Automated segmentation of normal and diseased coronary arteries—the asoca challenge. *Computerized Medical Imaging and Graphics* **97**, 102049 (2022)

11. de Haan, P., Weiler, M., Cohen, T., Welling, M.: Gauge equivariant mesh cnns: Anisotropic convolutions on geometric graphs. CoRR **abs/2003.05425** (2020), <https://arxiv.org/abs/2003.05425>
12. van Harten, L.D., de Jonge, C.S., Beek, K.J., Stoker, J., Išgum, I.: Untangling and segmenting the small intestine in 3d cine-mri using deep learning. *Medical Image Analysis* **78**, 102386 (2022)
13. Larrabide, I., Radaelli, A., Frangi, A.: Fast virtual stenting with deformable meshes: application to intracranial aneurysms. In: *Medical Image Computing and Computer-Assisted Intervention—MICCAI 2008: 11th International Conference, New York, NY, USA, September 6-10, 2008, Proceedings, Part II* 11. pp. 790–797. Springer (2008)
14. Lesage, D., Angelini, E.D., Bloch, I., Funka-Lea, G.: A review of 3d vessel lumen segmentation techniques: Models, features and extraction schemes. *Medical image analysis* **13**(6), 819–845 (2009)
15. Litjens, G., Ciompi, F., Wolterink, J.M., de Vos, B.D., Leiner, T., Teuwen, J., Išgum, I.: State-of-the-Art deep learning in cardiovascular image analysis. *JACC Cardiovasc Imaging* **12**(8 Pt 1), 1549–1565 (Aug 2019)
16. Lugauer, F., Zhang, J., Zheng, Y., Hornegger, J., Kelm, B.M.: Improving accuracy in coronary lumen segmentation via explicit calcium exclusion, learning-based ray detection and surface optimization. In: *Medical Imaging 2014: Image Processing*, vol. 9034, pp. 993–1002. SPIE (2014)
17. Ma, B., Han, Z., Liu, Y.S., Zwicker, M.: Neural-pull: Learning signed distance function from point clouds by learning to pull space onto surface. In: *International Conference on Machine Learning*. pp. 7246–7257. PMLR (2021)
18. Nibali, A., He, Z., Morgan, S., Prendergast, L.A.: Numerical coordinate regression with convolutional neural networks. CoRR **abs/1801.07372** (2018), <http://arxiv.org/abs/1801.07372>
19. van Praagh, G.D., Nienhuis, P.H., Reijrink, M., Davidse, M.E., Duff, L.M., Spottiswoode, B.S., Mulder, D.J., Prakken, N.H., Scarsbrook, A.F., Morgan, A.W., et al.: Automated multiclass segmentation, quantification, and visualization of the diseased aorta on hybrid pet/ct–sequoia. *Medical Physics* (2024)
20. Shani, U., Ballard, D.H.: Splines as embeddings for generalized cylinders. *Computer Vision, Graphics, and Image Processing* **27**(2), 129–156 (1984)
21. Shit, S., Paetzold, J.C., Sekuboyina, A., Zhylyka, A., Ezhov, I., Unger, A., Pluim, J.P.W., Tetteh, G., Menze, B.H.: cldice - a topology-preserving loss function for tubular structure segmentation. CoRR **abs/2003.07311** (2020), <https://arxiv.org/abs/2003.07311>
22. Taylor, C.A., Petersen, K., Xiao, N., Sinclair, M., Bai, Y., Lynch, S.R., Upde-Pac, A., Schaap, M.: Patient-specific modeling of blood flow in the coronary arteries. *Computer Methods in Applied Mechanics and Engineering* **417**, 116414 (2023). <https://doi.org/https://doi.org/10.1016/j.cma.2023.116414>, <https://www.sciencedirect.com/science/article/pii/S0045782523005388>, a Special Issue in Honor of the Lifetime Achievements of T. J. R. Hughes
23. Wasserthal, J., Breit, H.C., Meyer, M.T., Pradella, M., Hinck, D., Sauter, A.W., Heye, T., Boll, D.T., Cyriac, J., Yang, S., Bach, M., Segeroth, M.: Totalsegmentator: Robust segmentation of 104 anatomic structures in ct images. *Radiology: Artificial Intelligence* **5**(5), e230024 (2023). <https://doi.org/10.1148/ryai.230024>, <https://doi.org/10.1148/ryai.230024>
24. Wolterink, J.M., van Hamersvelt, R.W., Viergever, M.A., Leiner, T., Išgum, I.: Coronary artery centerline extraction in cardiac CT angiography using a cnn-

- based orientation classifier. CoRR **abs/1810.03143** (2018), <http://arxiv.org/abs/1810.03143>
25. Wolterink, J.M., Leiner, T., Išgum, I.: Graph convolutional networks for coronary artery segmentation in cardiac ct angiography. In: Graph Learning in Medical Imaging: First International Workshop, GLMI 2019, Held in Conjunction with MICCAI 2019, Shenzhen, China, October 17, 2019, Proceedings 1. pp. 62–69. Springer (2019)